DOI 10.24425/aee.2021.137573

Rotor optimization of axial-radial flux type synchronous machine based on magnetic flux leakage

HONGBO QIU, SHUBO ZHANG

Zhengzhou University of Light Industry
China
e-mail: ZSHUBO1205@163.com

(Received: 27.08.2020, revised: 06.03.2021)

Abstract: The axial-radial flux type permanent magnet synchronous machine (ARFTPMSM) can adjust the main magnetic field by controlling the axial flux, so it can overcome the problem that the flux of the permanent magnet synchronous motor (PMSM) is difficult to adjust. Due to the existence of the axial device in the ARFTPMSM, the finite element method (FEM) is used to establish a three-dimensional model for analysis. By analyzing the magnetic density distribution of the rotor, it is found that there is a serious magnetic leakage phenomenon at both ends of the tangential permanent magnet. The rotor material at the end of the tangent permanent magnet is replaced by non-ferromagnetic material to reduce the magnetic leakage. On this basis, the influence of the width of the non-ferromagnetic material on the performance of the motor is compared. By Fourier decomposition of the back-EMF waveform, the total harmonic distortion (THD) rate of the back-EMF under different axial magnetomotive force (MMF) was calculated. Finally, the eddy current distribution and the eddy current loss of the rotor are analyzed, and the variation law of the eddy current loss is summarized. The conclusion can provide reference for the optimal design of the ARFTPMSM.

Key words: ARFTPMSM, rotor structure, three-dimensional model, magnetic leakage

1. Introduction

The difference in excitation methods in motor design makes the output characteristics, power density, and efficiency of the motor very different. The electric excitation motor can easily adjust the air gap magnetic field by changing the excitation winding current, thereby realizing a wide range of output voltage regulation or speed regulation characteristics. However, due to the existence of excitation loss, the efficiency of the motor system is relatively low, and it is difficult

to achieve high power density [1]. The permanent magnet motor has no excitation winding, which eliminates the excitation loss and improves the efficiency of the motor [2, 3]. However, due to the inherent characteristics of the permanent magnet material, the air gap magnetic field of the permanent magnet motor is kept substantially constant. When the permanent magnet motor is working, it is often only possible to inject a large direct-axis current component through the armature winding to achieve the field weakening control, which limits the speed range of constant power and the application of the motor in some wide speed control fields [4–6].

Hybrid excitation motors (HEMs) strive to combine the high-efficiency and high-power density of permanent magnet motors and the convenience control of electric excitation motors, and become a focus in the field of motor research [7]. The HEM has two kinds of excitation sources, including electric excitation and permanent magnet excitation. The air gap magnetic density can be adjusted by controlling the magnitude and direction of the current in the electric excitation coil [8, 9]. Compared with the traditional magnetic adjustment method, the magnetic adjustment method of the HEM is simpler and more direct. When the magnetic regulation fails, the magnetic regulation method of the HEM will not damage the device such as the frequency converter and will discard the complicated calculation [10, 11]. In recent years, many scholars have in-depth research on the HEM. Professor Hua uses the hybrid excitation method to introduce the excitation winding into the flux-switching permanent magnet motor, which makes the air gap magnetic density of the motor adjustable [12]. Professor Wang added an axial stator to the axial direction of the PMSM to achieve a wide range of magnetic regulation by controlling the current component in the armature winding and axial winding [13]. Compared with [13], the ARFTPMSM is provided with a DC winding in the axial direction, and the main magnetic field is regulated by controlling the direct current, which simplifies the flux regulation method. There are many researches on optimization of magnetic the flux leakage of PMSM in the world, but there are relatively few researches on optimization of magnetic flux leakage of HEMs [14, 15]. This paper focuses on the optimal design of ARFTPMSM magnetic flux leakage.

In reference [16], the rotor structure of the ARFTPMSM is analyzed, and the blocking effect of the radial permanent magnet on flux regulation is studied. On this basis, the flux regulation characteristics and eddy current loss of the motor are analyzed when the rotor only retains the tangential permanent magnet. Compared with reference [16], this paper focuses on the magnetic leakage of the permanent magnet in the rotor. By optimizing the leakage region at the end of the tangential permanent magnet, the utilization ratio of the permanent magnet is greatly increased, and the field adjustment range of the motor is increased to a certain extent.

Flux leakage optimization is an important aspect for motor improvement, which can improve the utilization rate of magnetic flux and save the consumption of the permanent magnet. In the optimization of HEMs, many scholars have made great efforts in the optimization of flux leakage and increasing the range of flux regulation. Hu Wenjing studied the magnetic flux leakage problem of HEMs and obtained the optimal flux density distribution [17]. By optimizing the axial air gap, Professor Zhang Zhuoran increased the field adjusting range of the HEM [18]. On the basis of optimizing the magnetic flux leakage, this paper compares the changes of the magnetic flux adjustment range of the motor, and the results show that the optimization measures can not only effectively improve the magnetic flux leakage of the motor, but also increase the magnetic flux adjustment range of the motor to a certain extent. In this paper, the problem of rotor magnetic flux leakage was studied, and non-ferromagnetic materials are used to optimize the phenomenon

of rotor magnetic flux leakage. The three-dimensional finite element model of rotor structure is constructed, the air gap magnetic density and the back EMF of the three rotor structures under different excitation magnetic potentials are compared, and the magnetic adjustment range is determined. On this basis, the variation of harmonic content and eddy current loss under different axial magnetomotive force (MMF) is studied.

2. ARFTPMSM structure and working principle

Unlike conventional PMSMs, ARFTPMSMs add axial excitation devices at both ends of the PMSM. The structure of the ARFTPMSM is showed in Fig. 1. The ARFTPMSM consists of three parts: a stator part, a rotor part and an axial excitation part. The stator part includes a stator core and an armature winding. The rotor part is composed of a rotor core, a permanent magnet and an NS ferromagnetic bridge. The N ferromagnetic bridge and the S ferromagnetic bridge are composed of five claw poles and a ring, respectively. The claw poles of the N ferromagnetic bridge and the S ferromagnetic bridge are staggered on the rotor, evenly distributed on the N and S poles of the rotor and rotate with the rotor. The axial excitation part includes an end cap and an axial excitation coil, and the axial excitation coil is placed in the end cap. The main air gap magnetic density can be adjusted by controlling the magnitude and direction of the direct current. In addition, because the two axial excitation devices are located at both ends of the motor, the direction of the current should be opposite when the air gap flux density is adjusted together.

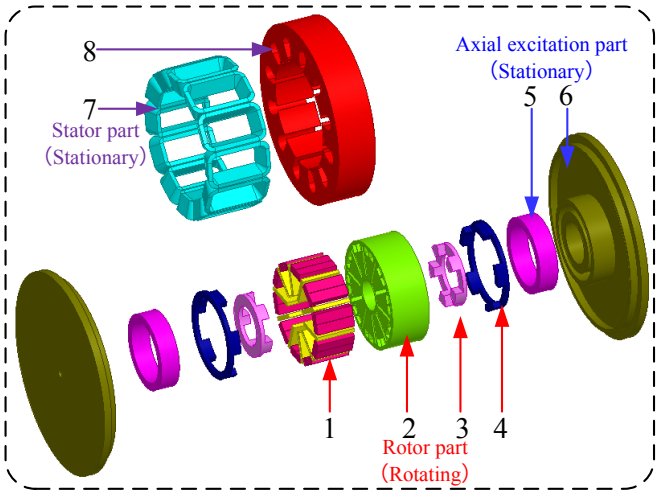

Fig. 1. Structure of ARTFPMSM: 1 permanent magnet; 2 rotor core; 3 S ferromagnetic bridge; 4 N ferromagnetic bridge; 5 axial excitation coil; 6 end cap; 7 armature windings; 8 stator core

The working principle of the ARFTPMSM is shown in Fig. 2. When there is no current in the axial excitation coil, only the magnetic field generated by the permanent magnet exists in the

motor. The permanent magnet flux forms an axial closed magnetic circuit and a radially closed magnetic circuit in the axial/radial direction, and the specific direction is as shown in Fig. 2(a).

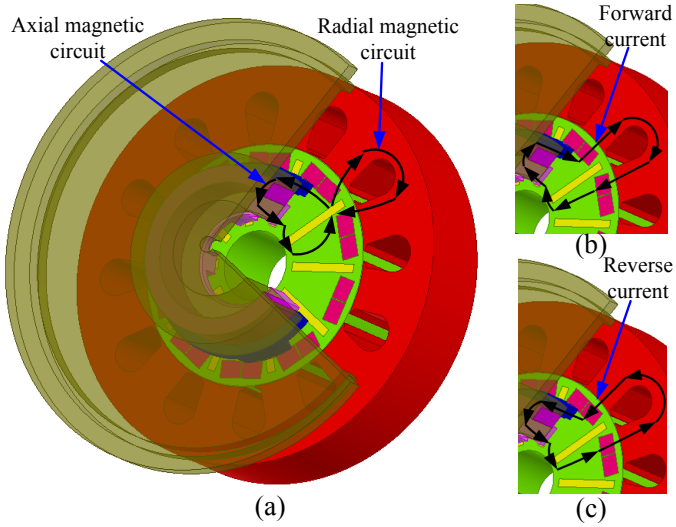

Fig. 2. Magnetic flux paths: (a) permanent magnet magnetic circuit; (b) forward current magnetic circuit; (c) reverse current magnetic circuit

As shown in Fig. 2(b), when the current in the axial excitation coil is positive, the electric excitation coil generates axial flux. The magnetic flux direction of the magnetic circuit is opposite to the axial magnetic circuit of the permanent magnet flux, which is consistent with the radial magnetic circuit of the permanent magnet flux. Then the radial flux is enhanced and the axial flux is weakened.

As shown in Fig. 2(c), when the reverse current is in the axial excitation coil, the direction of the flux generated by the electric excitation coil is the same as that of the axial magnetic circuit of the permanent magnet, and is opposite to the direction of the radial magnetic circuit. Then the radial air gap magnetic density is weakened and the axial air gap magnetic density is enhanced. Table 1 lists the basic parameters of the ARFTPMSM. Table 2 shows the materials

Table 1. Parameters of ARTFPMSM

Parameters	**units**	**Value**
Rated power	kW	3.5
Rated speed	r/min	250
Rotor axial length	mm	50
Stator inner diameter	mm	140
Stator outer diameter	mm	230
Slot number	–	12

of each component of the motor. It should be noted that considering that the rotor should have good axial permeability and mechanical strength, the solid rotor is adopted, and the rotor material is m20.

Table 2. Material of each part of the ARFTPMSM

Component	Material
Stator core	DW310
Rotor core	m20
Ferromagnetic bridge	m20
End cap	m20
Permanent magnets	N35
Armature winding	copper
Axial excitation windings	copper

3. Optimization and comparison of rotor structure

3.1. Magnetic flux leakage optimization design

The magnetic pole structure of the ARFTPMSM is a hybrid magnetic pole arrangement. The hybrid magnetic pole arrangement can increase the air gap magnetic density of the motor and increase the overload capacity. The magnetic pole arrangement structure is shown in Fig. 3.

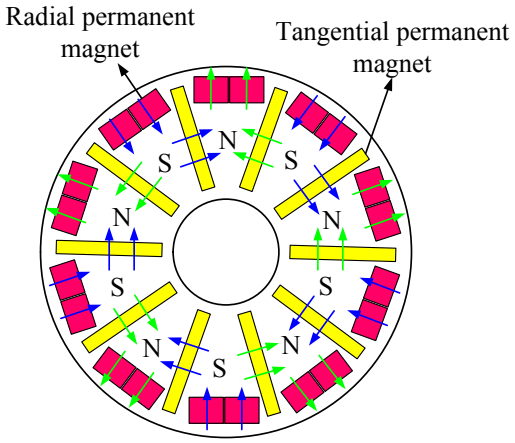

Fig. 3. Magnetic pole arrangement

If the magnetic flux leakage in the rotor is serious, it will affect the utilization of the permanent magnet. As shown in Fig. 4(a), it is the magnetic density of the rotor when the axial MMF is 0 AT. It can be seen that the original rotor structure has a large magnetic flux leakage phenomenon at

both ends of the tangential permanent magnet, which causes the flux saturation at both ends of the tangential permanent magnet and reduces the utilization rate of the permanent magnet. In Fig. 4(b), by replacing the rotor material at the end of the the tangential permanent magnet with non-ferromagnetic material in the ARFTPMSM, the leakage flux of the permanent magnet in the ARFTPMSM is reduced, and the flux utilization rate of the permanent magnet is also increased.

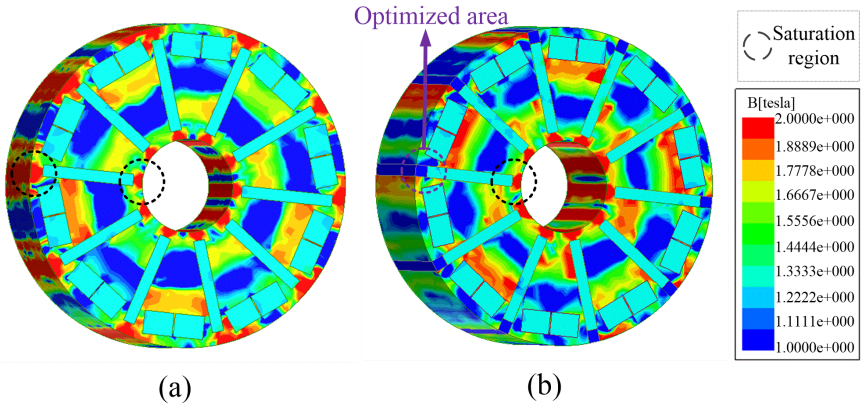

Fig. 4. Rotor flux density at 0 AT excitation potential: (a) original rotor structure; (b) improved rotor structure

The optimized scheme for reducing magnetic flux leakage is shown in Fig. 5. The thickness of the non-ferromagnetic material at the end of the tangential permanent magnet is set to 5 mm. In the optimal design of the motor rotor, the non-magnetic material can be replaced by resin. In order to ensure the reliability and safety of the motor, carbon fiber with a thickness of 1 mm can be wound on the outside of the rotor.

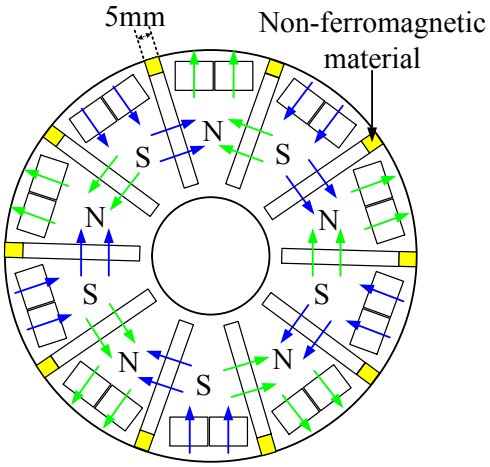

Fig. 5. Magnetic flux leakage optimization scheme

3.2. Comparison of rotor structure

Based on the above analysis, the optimized structure is compared with the original rotor structure. By establishing a three-dimensional finite element analysis model, the magnetic regulation performance of the ARFTPMSM under two kinds of rotor structures was compared. Fig. 6 shows the air gap magnetic density and no-load back EMF of the two rotor structures under different axial MMF. Fig. 6(a) shows the air gap magnetic density of the machine under different axial MMF. It can be seen from the figure that the flux density increases significantly after the optimized magnetic flux leakage, and the adjustment range of the flux increases by 0.06 T.

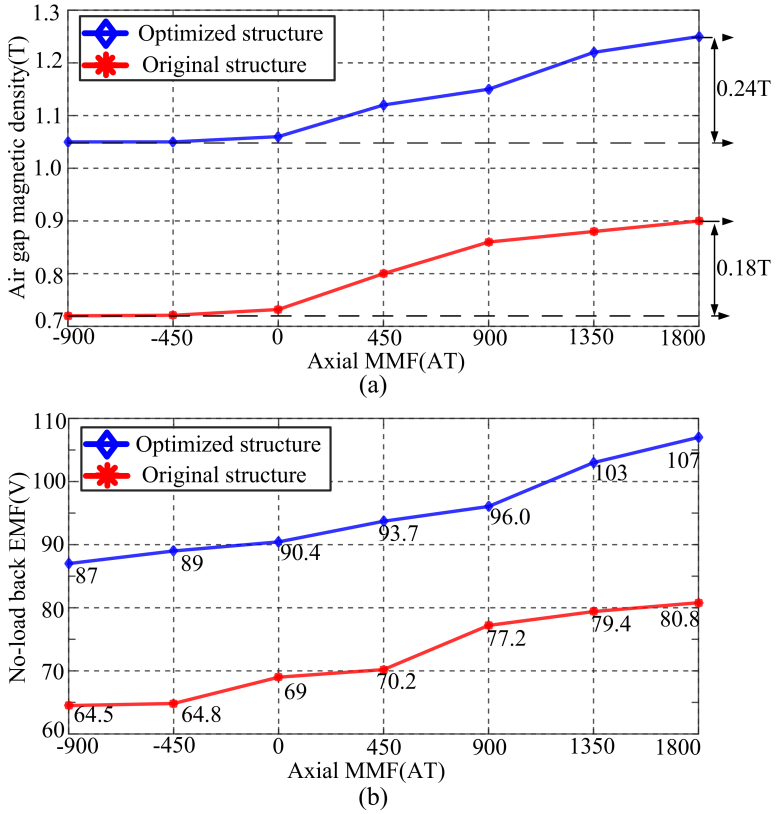

Fig. 6. Variation of air gap magnetic density and no-load back EMF under different axial MMF

The air gap flux density directly affects the no-load back EMF of the motor, and there is a positive correlation between them. Fig. 6(b) shows the no-load EMF of the machine under different axial MMF. It can be seen from Fig. 6(b) that the variation law of no-load back EMF of the motor under three rotor structures is consistent with that of air gap flux density, which proves the correctness of the analysis law of air gap flux density. Under the 0 AT axial MMF, the no-load back-EMF after the motor optimization is 21.4 V higher than the original structure.

3.3. Effect of non-ferromagnetic material width on motor performance

Through the above analysis, it is found that the application of non-ferromagnetic materials not only improves the utilization rate of permanent magnets, but also improves the magnetic adjustment range. In order to explore the influence of non-ferromagnetic materials on the change of magnetic regulation, the influence of the width of non-ferromagnetic materials on the range of magnetic regulation was studied. Table 3 shows the change of air gap magnetic density under different axial MMF. In order to verify the accuracy of the change of air gap magnetic density, Table 4 lists the change of no-load back EMF of the ARFTPMSM.

Table 3. Change of air gap magnetic density

Width	**Axial MMF (AT)**							**Variation range of flux density (T)**
	–900	–450	0	450	900	1350	1800	
0 mm	0.72	0.721	0.732	0.80	0.86	0.88	0.90	0.18
1 mm	0.89	0.90	0.91	0.96	1.0	1.04	1.05	0.16
3 mm	1.0	1.01	1.02	1.04	1.11	1.17	1.20	0.20
5 mm	1.05	1.06	1.08	1.12	1.15	1.22	1.29	0.24

Comparing the data in Table 3 and Table 4, it can be found that as the width of non-ferromagnetic materials increases, the magnetic leakage phenomenon is more significantly reduced, the magnetic flux utilization rate is improved, and the air gap magnetic density and no-load back-EMF become larger. However, the addition of non-ferromagnetic materials does not necessarily increase the magnetic regulation range of the motor. When the non-ferromagnetic material is 1mm, the magnetic regulation performance of the motor will decline. Then with the increase of the width of the non-ferromagnetic material, the magnetic adjustment range becomes larger. When the width of the non-ferromagnetic material is 5 mm, the magnetic adjustment range is increased by 0.06 T compared with the original structure, and the magnetic adjustment range is increased by 33%.

Table 4. Change of no-load back EMF

Width	**Axial MMF (AT)**							**Variation range of no-load back EMF (V)**
	–900	–450	0	450	900	1350	1800	
0 mm	64.48	64.83	69.0	70.2	77.2	79.36	80.76	16.28
1 mm	73.9	73.32	75.19	78.11	83.27	85.58	87.75	13.85
3 mm	85.0	85.02	87.0	87.8	93.0	99.0	103.04	18.04
5 mm	87.0	89.0	90.44	93.71	96.05	103.0	107.0	20

The working state of the motor under load is particularly important, so the power factor of the motor under rated load is compared. Table 5 lists the power factors of motors with different

optimized structures. As can be seen from Table 5, the power factors of different rotor structures are close to 1 when the motor operates under rated load, and it is in a good working state. This indicates that the motor efficiency is higher under different rotor structures.

Table 5. Power factors of motors with different optimized structures

Width	**0 mm**	**1 mm**	**3 mm**	**5 mm**
Power factor	0.95	0.96	0.96	0.96

The optimization of rotor flux leakage region affects the magnetic field distribution in the motor, and then affects the torque ripple of the motor. In order to compare the motor output torque under different rotor structures, the torque fluctuation coefficient was compared. The calculation formula of the torque fluctuation coefficient is

$$K_{mb} = \frac{T_{\max} - T_{\min}}{T_{\max} + T_{\min}} \times 100\%. \tag{1}$$

When the motor works in the third quadrant, the load is set at 27.1 N·m [19]. According to the calculation formula of the torque fluctuation coefficient, the torque ripple coefficient under different rotor structures is obtained. The specific results are shown in Table 6. Fig. 7 is the torque waveform under different rotor structures. Combined with Table 6 and Fig. 7, it can be seen that the torque fluctuation coefficient of the motor is large, which is mainly due to the winding mode of the centralized winding and the shunt effect of the axial excitation device on permanent magnet flux, which makes the air gap magnetic density of the motor uneven, thus affecting the torque fluctuation. It can also be seen from Table 6 that after optimizing the flux leakage area, the torque

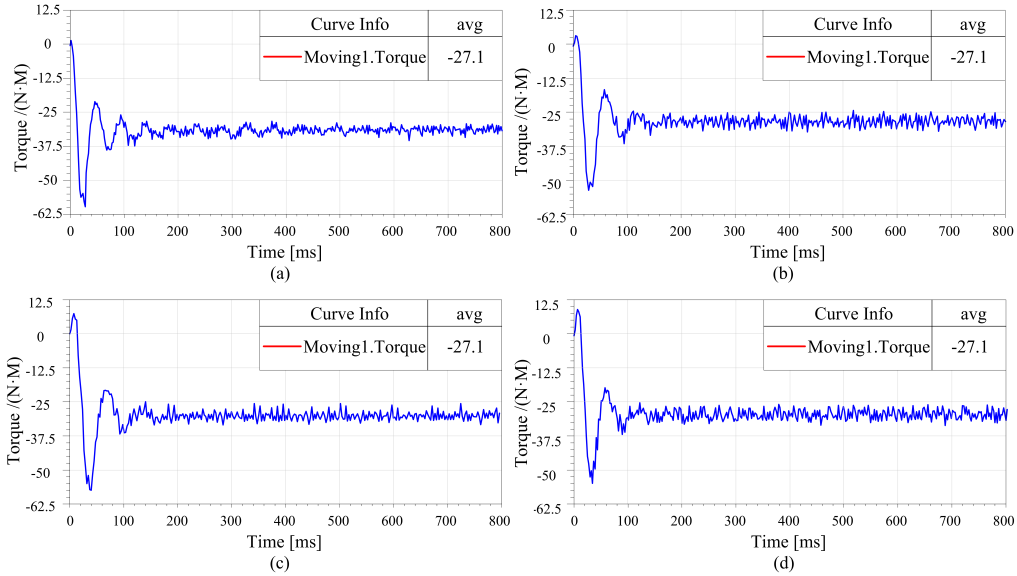

Fig. 7. Torque waveform under different rotor structures

ripple coefficient of the motor increases, and with the increase of the width of the optimization area, the torque fluctuation coefficient begins to increase. Therefore, the optimized width and torque fluctuation coefficient of permanent magnets should be considered in practical design.

Table 6. Torque ripple coefficient under different rotor structures

Width	**0 mm**	**1 mm**	**3 mm**	**5 mm**
Torque ripple coefficient (%)	6.2	9.2	9.8	10.2

3.4. Harmonic analysis of no-load back EMF

The harmonic content of the back EMF has a great influence on the heating, torque fluctuation and efficiency of the motor. Therefore, the harmonic content of no-load back EMF is further analyzed, and the influence of different width of non-ferromagnetic materials on the motor efficiency is obtained. The formula for calculating the total harmonic distortion (THD) rate of back EMF is as follows [20]:

$$\mathrm{THD} = \frac{\sqrt{\dfrac{1}{T}\displaystyle\int_r \left(\sum_{n=2}^{\infty} E_n \sin(n\omega t + \alpha_n)\right)^2 \mathrm{d}t}}{\sqrt{\dfrac{1}{T}\displaystyle\int_r \left(E_1 \sin\left(n\omega t + \alpha_1\right)\right)^2 \mathrm{d}t}} \times 100\%, \tag{2}$$

where: E_n is the rms value of the n order harmonic back EMF, E_1 is the rms value of the back EMF fundamental content.

Fig. 8 shows the change of the THD of no-load back EMF under the no-load state of the motor. It can be seen from the figure that the addition of non-ferromagnetic materials increases the harmonic content when the axial MMF is 0 AT, and with the increase of the width of non-ferromagnetic materials, the harmonic content gradually decreases. With the change of the axial

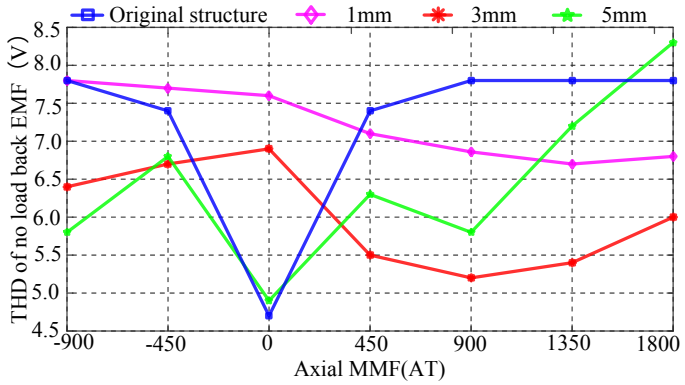

Fig. 8. THD of no-load back EMF

MMF, the harmonic content of the original structure increases obviously. However, in the scheme of adding non ferromagnetic materials, the harmonic content has become smaller than the original structure. When the axial MMF is increased from 450 AT to 1800 AT, the harmonic content is the smallest when the width of the non-ferromagnetic material is 3 mm. Fig. 9 shows the waveform of the back EMF when the axial MMF is 0 AT. It can be seen that the sinusoidal degree of no-load back EMF is the best under the original structure.

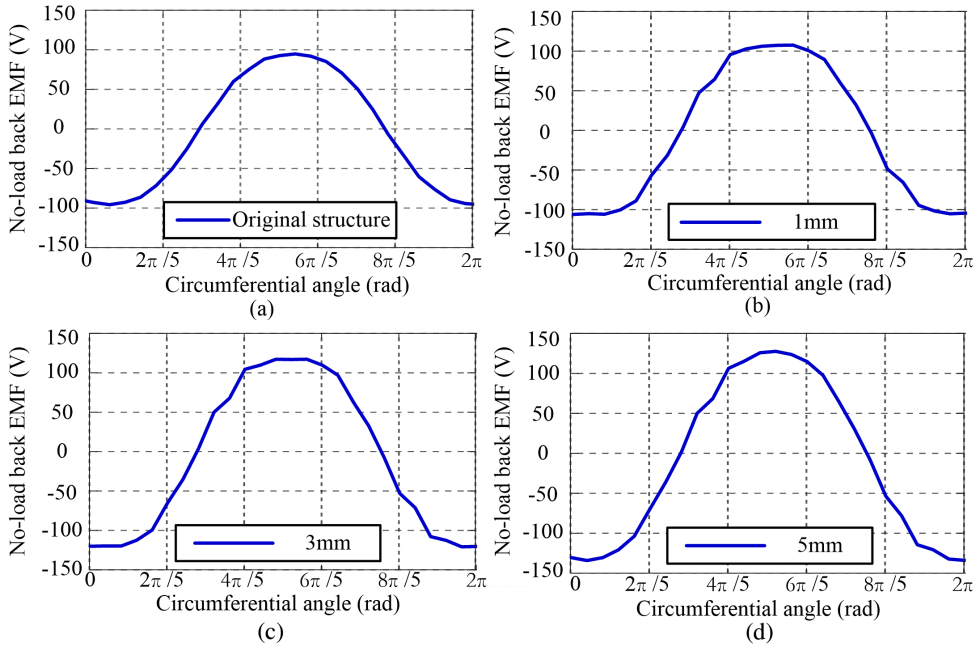

Fig. 9. No-load back EMF waveform of non-ferromagnetic materials with different width: (a) original structure; (b) 1 mm; (c) 3 mm; (d) 5 mm

4. Eddy current loss analysis

The eddy current of the rotor in the motor makes the rotor generate heat seriously, the loss increases, and the permanent magnet on the rotor may be demagnetized. Therefore, the analysis of the eddy current distribution of the motor is very important. Fig. 10 shows the eddy current distribution of three rotor structures under different axial MMF when the motor is running stably.

When the excitation magnetic potential is 0 AT, the maximum values of the eddy current density of the four rotor structures are 1.04×10^6 A/m^2, 3.9×10^6 A/m^2, 4.02×10^6 A/m^2 and 1.18×10^6 A/m^2, 2.39×10^6 A/m^2. When the axial excitation magnetic potential is 1350 AT, the maximum value of the eddy current rises rapidly, and the maximum eddy current density of the three rotor structures reaches 2.21×10^6 A/m^2, 1.33×10^7 A/m^2, 1.56×10^7 A/m^2, and 2.49×10^7 A/m^2.

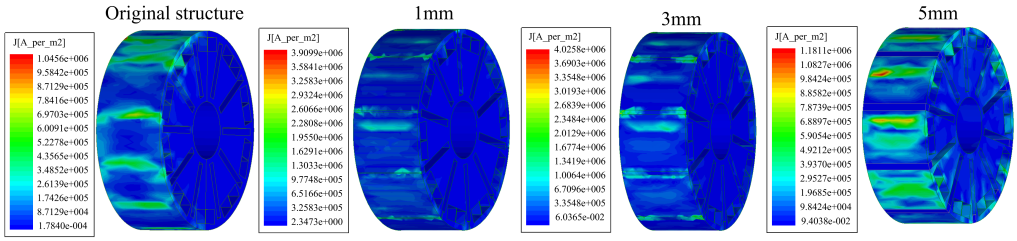

(a)

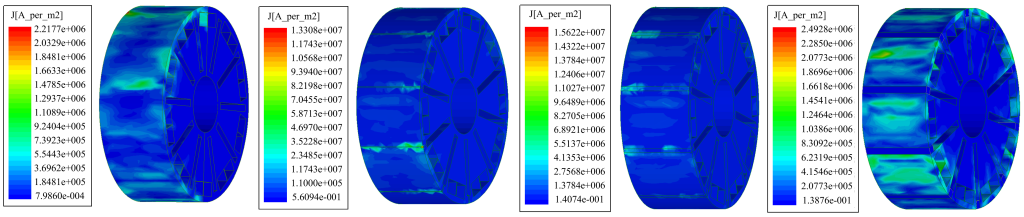

(b)

Fig. 10. Eddy current loss under different excitation potential: (a) 0 AT excitation potential; (b) 1350 AT excitation potential

During the operation of the motor, due to the existence of space harmonic and time harmonic generated by stator teeth and PWM power supply, the rotating speed is different from that of the rotor, so induction electromotive force and rotor eddy current will be generated on the rotor, which will produce eddy current loss. The heat caused by the rotor eddy current has a great influence on the structural strength of the rotor and the demagnetization of the permanent magnet. Therefore, based on the finite element analysis, the eddy current distribution of the rotor is analyzed in the steady state. The calculation formula of eddy current loss is [21]

$$P_e = \frac{1}{T_e} \int_{T_e} \int_{vol} \frac{1}{\sigma_r} J^2 \, \mathrm{d}V \, \mathrm{d}t, \tag{3}$$

where: P_e represents the rotor eddy current losses (in watts), J is the current density in each element (in ampere per square meter), σ_r is the conductivity of the eddy current zone (in siemens per meter), T_e is the cycle of time, and vol is the region of eddy current losses.

According to the above calculation method, the eddy current loss of the motor is calculated. Fig. 11 shows the eddy current loss of the rotor under different axial MMF. The data is calculated by the FEM when the motor is running at no-load. It can be seen from the figure that the eddy current loss of the motor is smaller when there is no non-ferromagnetic material for the rotor, and it is obviously larger when there is non-ferromagnetic material. The influence of non-ferromagnetic materials on eddy current loss is the same in different width, and the variation law of the eddy current loss curve is the same.

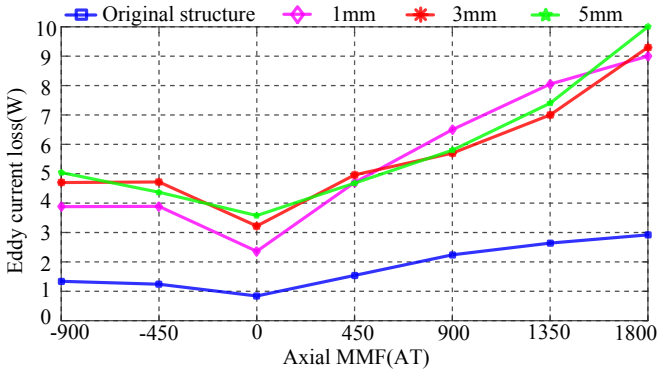

Fig. 11. Eddy current loss under different rotor structures

5. Experimental verification and analysis

In order to verify the correctness of the data analysis, the no-load back EMF of the motor is compared through experiments. As shown in Fig. 12, it is the prototype of the ARTFPMSM. Fig. 13 shows the test platform of the motor. The no-load back-EMF of the motor can be obtained by driving the prototype machine at 250 r/min speed.

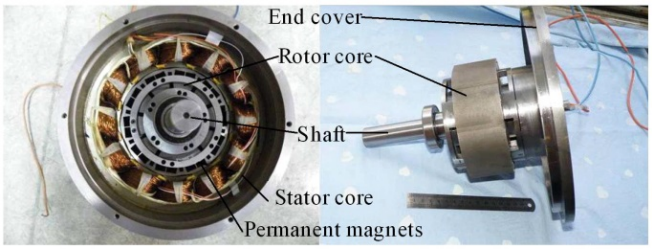

Fig. 12. The ARTFPMSM prototype

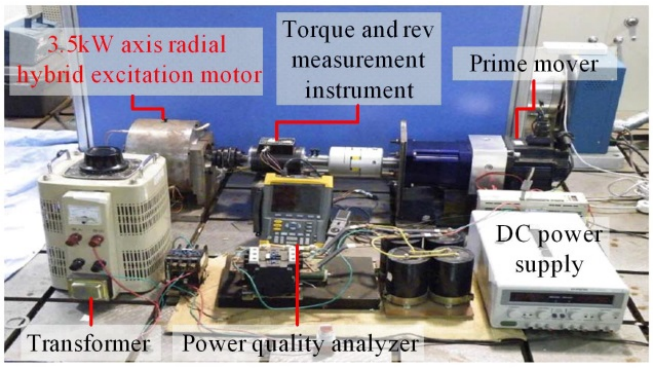

Fig. 13. The experiment platform

The non-load back EMF of the prototype is measured by a power quality analyzer, and the data is shown in Fig. 14. It should be noted that the experimental data is the line voltage. In the experimental data, when the axial MMF is 0 AT, the maximum peak voltage of the line is 180 V, the minimum peak value is 178 V, and the line voltage RMS is 126 V. When the axial MMF is 900 AT, the maximum peak value is 192 V, the minimum peak value is 190 V, and the line voltage RMS is 133 V. When the axial MMF is 1350 AT, the maximum peak value is 194 V, the minimum peak value is 192 V, and the line voltage RMS is 135 V. The comparison between the measured data and the calculated results is shown in Table 7. The error between the experimental results and the calculated results is less than 5%, within a reasonable range.

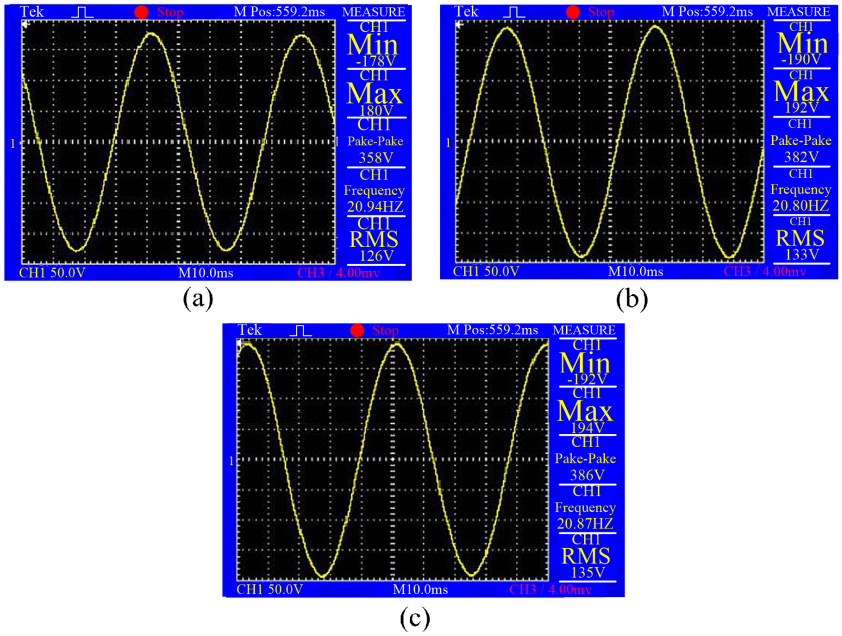

Fig. 14. ARFTPMSM line-line voltage waveforms: (a) axial MMF of 0 AT; (b) axial MMF of 900 AT; (c) axial MMF of 1350 AT

Table 7. The comparison of measured data and calculated results

Excitation potential (AT)	**Phase non-load back EMF (phase voltage)**	
	Measured data (V)	**Calculated result (V)**
0	72.7	69.0
900	77.9	77.2
1350	79.21	79.36

6. Conclusions

In this paper, by analyzing the magnetic flux density of the rotor, it is found that the magnetic leakage at the end of the tangential permanent magnet is relatively serious. By replacing the rotor material at the end of the tangential permanent magnet with a non-ferromagnetic material, the magnetic leakage of the permanent magnet is reduced. On this basis, the effect of non-ferromagnetic material width on motor performance was further compared, and the following conclusions were reached:

1. By replacing the rotor material at the end of the tangential permanent magnet with a non-ferromagnetic material, the magnetic leakage of the permanent magnet is reduced, and the utilization rate of the permanent magnet is improved. With the increase of the width of the non-ferromagnetic material, the leakage is reduced more obviously.
2. When the non-ferromagnetic material is added to the end of the tangent permanent magnet, the adjustment range of the magnetic field increases with the increase of the width of the non-ferromagnetic material. When the width of the non-ferromagnetic material is 5 mm, the adjusting range of the magnetic field is 33% higher than that of the original structure.
3. When the axial MMF is 0 AT, the THD of the no-load back EMF of the motor increases when the non-ferromagnetic material is added to the rotor, but with the increase of the axial MMF, the THD of the no-load back EMF becomes smaller than the original structure. When the axial MMF is 450 AT to 1800 AT, the THD of back EMF is the smallest when the width of the non-ferromagnetic material is 3 mm.
4. After adding the non-ferromagnetic material to the end of the tangential permanent magnet, the eddy current loss of the rotor becomes larger than the original structure, and the variation of eddy current loss in different width of non-ferromagnetic materials is consistent.

References

[1] Zhao X., Niu S., Ching T.W., *Design and Analysis of a New Brushless Electrically Excited Claw-Pole Generator for Hybrid Electric Vehicle*, in IEEE Transactions on Magnetics, vol. 54, no. 11, pp. 1–5 (2018).

[2] Sathyan Sabin *et al*., *Influence of Magnetic Forces and Magnetostriction on the Vibration Behavior of an Induction Motor*, pp. 825–834 (2019).

[3] Hongbo Qiu, Yong Zhang *et al*., *Performance Analysis and Comparison of PMSM with Concentrated Winding and Distributed Winding [J]*, Archives of Electrical Engineering, vol. 69, no. 2, pp. 303–317 (2020).

[4] Kommuri S.K., Defoort M., Karimi H.R., Veluvolu K.C., *A Robust Observer-Based Sensor Fault-Tolerant Control for PMSM in Electric Vehicles*, in IEEE Transactions on Industrial Electronics, vol. 63, no. 12, pp. 7671–7681 (2016).

[5] Liu X., Chen H., Zhao J., Belahcen A., *Research on the Performances and Parameters of Interior PMSM Used for Electric Vehicles*, in IEEE Transactions on Industrial Electronics, vol. 63, no. 6, pp. 3533–3545 (2016).

[6] Tong W. *et al*., *Feasibility Analysis of 100 kA DC Commutation Scheme to be Applied in the Quench Protection Unit of CFETR*, in IEEE Transactions on Applied Superconductivity, vol. 30, no. 1, pp. 1–9 (2020).

[7] Yıldırız E., Onbilgin G., *Comparative study of new axial field permanent magnet hybrid excitation machines*, in IET Electric Power Applications, vol. 11, no. 7, pp. 1347–1355 (2017).

[8] Weili L., Hongbo Q., Ran Y., Xiaochen Z., Liyi L., *Three-Dimensional Electromagnetic Field Calculation and Analysis of Axial–Radial Flux-Type High-Temperature Superconducting Synchronous Motor*, IEEE Trans. Appl. Supercond., vol. 23, no. 1, article sequence number 5200607 (2013).

[9] Zhang Z., Liu Y., Tian B., Wang W., *Investigation and Implementation of a New Hybrid Excitation Synchronous Machine Drive System*, IET Electric Power Application, vol. 11, no. 4, pp. 487–494 (2017).

[10] Kim K., *A Novel Magnetic Flux Weakening Method of Permanent Magnet Synchronous Motor for Electric Vehicles*, in IEEE Transactions on Magnetics, vol. 48, no. 11, pp. 4042–4045 (2012).

[11] Kim D.Y., Jang G.H., Nam J.K., *Magnetically Induced Vibrations in an IPM Motor Due to Distorted Magnetic Forces Arising From Flux Weakening Control*, in IEEE Transactions on Magnetics, vol. 49, no. 7, pp. 3929–3932 (2013), DOI: 10.1109/TMAG.2013.2238614.

[12] Hua W., Cheng M., Zhang G., *A Novel Hybrid Excitation Flux-Switching Motor for Hybrid Vehicles*, in IEEE Transactions on Magnetics, vol. 45, no. 10, pp. 4728–4731 (2009).

[13] Wang D., Zhang D., Xue D., Peng C., Wang X., *A New Hybrid Excitation Permanent Magnet Machine with an Independent AC Excitation Port*, in IEEE Transactions on Industrial Electronics, vol. 66, no. 8, pp. 5872–5882 (2019).

[14] Lee J. *et al*., *A Study on Analysis of Synchronous Reluctance Motor Considering Axial Flux Leakage Through End Plate*, in IEEE Transactions on Magnetics, vol. 55, no. 6, pp. 1–4, article sequence number 8201704 (2019).

[15] Ye X., Zheng S., Zhang Y., He Z., *Modeling and Optimization of IRTMB for High-Speed Motor Considering Magnetic Flux Leakage Effect*, 2019 22nd International Conference on Electrical Machines and Systems (ICEMS), Harbin, China, pp. 1–5 (2019).

[16] Qiu H., Yu W., Tang B., Mu Y., Li W., Yang C., *Study on the Influence of Different Rotor Structures on the Axial-Radial Flux Type Synchronous Machine*, in IEEE Transactions on Industrial Electronics, vol. 65, no. 7, pp. 5406–5413 (2018), DOI: 10.1109/TIE.2017.2784339.

[17] Hu W., Zhang X., Lei Y., Du Q., Shi L., Liu G., *Analytical Model of Air-Gap Field in Hybrid Excitation and Interior Permanent Magnet Machine for Electric Logistics Vehicles*, in IEEE Access, vol. 8, pp. 148237–148249 (2020), DOI: 10.1109/ACCESS.2020.3015601.

[18] Ma S., Zhang Z., *Investigation of field regulation characteristic of a hybrid excitation synchronous machine with axial auxiliary air-gaps*, 2012 15th International Conference on Electrical Machines and Systems (ICEMS), Sapporo, pp. 1–6 (2012).

[19] Jiang X., Xu D., Gu L., Li Q., Xu B., Li Y., *Short-Circuit Fault-Tolerant Operation of Dual-Winding Permanent-Magnet Motor Under the Four-Quadrant Condition*, in IEEE Transactions on Industrial Electronics, vol. 66, no. 9, pp. 6789–6798 (2019), DOI: 10.1109/TIE.2018.2878131.

[20] Hongbo Q., Ran Y., Weili L., Nan J., *Influence of rectifiers on high speed permanent magnet generator electromagnetic and temperature fields in distributed power generation systems*, IEEE Transactions on Energy Conversion, vol. 30, no. 2, pp. 655–662 (2015), DOI: 10.1109/TEC.2014.2366194.

[21] Weili L., Hongbo Q., Ran Y., Xiaochen Z., Liyi L., *Three-Dimensional Electromagnetic Field Calculation and Analysis of Axial–Radial Flux-Type High-Temperature Superconducting Synchronous Motor*, in IEEE Transactions on Applied Superconductivity, vol. 23, no. 1, article sequence number 5200607 (2013), DOI: 10.1109/TASC.2012.2232923.